




High-temperature deformation behavior and processing map of the as-cast Inconel 625 alloy

Zhi Jia* , Ze-Xi Gao, Jin-Jin Ji, De-Xue Liu, Ting-Biao Guo, Yu-Tian Ding

Received: 7 March 2019/Revised: 4 July 2019/Accepted: 25 May 2020/Published online: 2 July 2020
© The Nonferrous Metals Society of China and Springer-Verlag GmbH Germany, part of Springer Nature 2020

Abstract A short process of Inconel 625 alloy tube was developed to solve the problems of the traditional extrusion process, and particular attention was paid on the hot deformation behavior of the as-cast Inconel 625 alloy. The hot compression experiments were performed to study the hot deformation behavior of Inconel 625 in the temperature range of 900–1200 °C and strain rate range of 0.01–10.00 s⁻¹ by Gleeble-3500. The hot compressed microstructure was examined to study the effects of temperature and strain rate on the microstructural characteristic by electron backscatter diffraction (EBSD). The results show that the processing maps were greatly influenced by the temperature rather than the strain rate. It is found that with the strain increasing, the instability zone gradually turned to the low-temperature and low strain rate area, while the range of high-temperature instability area shrank. The optimum condition of the as-cast Inconel 625 alloy was determined as high strain rate region (temperature of 1100–1200 °C, strain rate of 1.00–10.00 s⁻¹) with the dissipation efficiency of above 0.28. As illustrated by microstructural characteristic of EBSD analysis, the perfect dynamic recrystallization occurred and fine grain structure was obtained under this deformation conditions.

Keywords Inconel 625; Hot deformation behavior; Constitutive equation; Microstructure; Processing map

1 Introduction

As a kind of Ni-based superalloy, Inconel 625 alloy has about 60% nickel content [1–4]. The initial development of the Inconel 625 alloy was intended to meet the high strength of the main steam tube [5–7]. Afterward, due to superior corrosion resistance, oxidation resistance, good creep properties, the fatigue properties, microstructural stability and excellent high-temperature mechanical properties, Inconel 625 alloy has been widely used within structural components, power plant of aeroengine, nuclear industry, chemical equipment and spraying [8–10].

The traditional extrusion process of Inconel 625 alloy tubes was displayed, as shown in Fig. 1a. However, long process, large energy consumption, complicated process of cogging, the brittle fracture and many defects were inevitable in this process [11, 12]. In order to solve these problems, a short process of Inconel 625 alloy tube was developed, as illustrated in Fig. 1b. Compared with the traditional hot extrusion process, the new process cancels the cogging process and greatly shortens the processing time to reduce the energy consumption. At present, the new process has achieved obvious results in actual production.

In addition, the deformation behavior and forming process of the Inconel 625 alloy are complex because of the large deformation resistance and the narrow range of hot forming parameters. At present, a lot of reports have been demonstrated on the deformation behavior, plastic mechanical properties and microstructural evolution with different deformation conditions. At high temperatures, the

Z. Jia*, Z.-X. Gao, D.-X. Liu, T.-B. Guo, Y.-T. Ding
School of Material Science and Engineering, Lanzhou University of Technology, Lanzhou 730050, China
e-mail: jjazhi1985@163.com

Z. Jia, D.-X. Liu, T.-B. Guo, Y.-T. Ding
Key State Key Laboratory of Advanced Processing and Recycling of Nonferrous Metals, Lanzhou University of Technology, Lanzhou 730050, China

J.-J. Ji
School of Materials Engineering, Lanzhou Institute of Technology, Lanzhou 730050, China

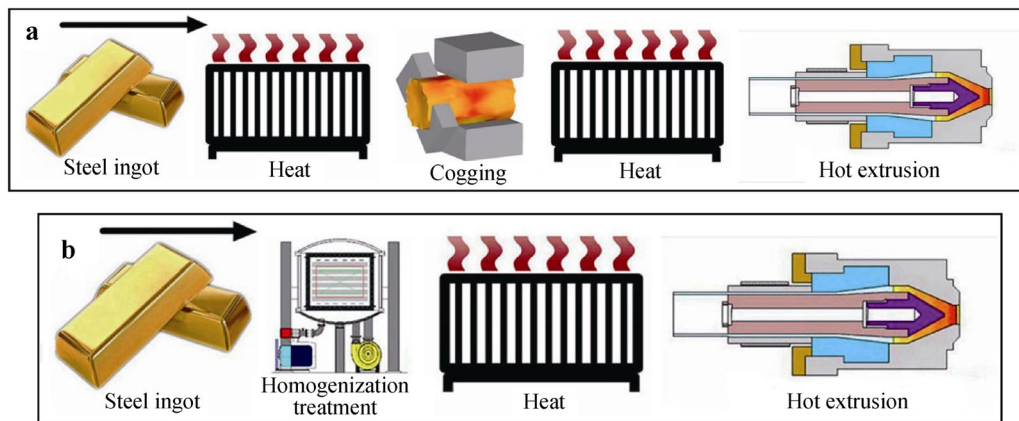


Fig. 1 **a** Traditional extrusion technology; **b** short flow extrusion process for Inconel 625 alloy tubes

grain growth behavior of Inconel 625 alloy was studied [13]. The results show that the fine crystals microstructure of Inconel 625 alloy increases significantly with the increase in temperature. Scanning electron microscope (SEM), X-ray diffraction (XRD) and chemical analysis method were carried out to illustrate the effect of W and Mo addition on the microstructure and mechanical properties of GY200 alloy [14]. Based on the extrusion technology of large-scale thick-walled Inconel 625 alloy pipe, the influence rule of process parameters on forming and the forming limit map Inconel 625 alloy were determined [15]. The microstructure, hardness and tensile properties of multiphase $V_{100-2x}-Ti_x-Ni_x$ ($x = 10, 15, 20$) alloys for hydrogen separation were investigated [16]. Microstructures and mechanical properties of Mg alloys extruded at various deformation conditions were investigated [17, 18]. Specially, some reports focused on the dynamic recrystallization behavior during hot deformation were studied [19–24]. The study found that the grain size and the recrystallization volume fraction increased with the increase in temperature, and the deformation began at the original twin grain boundaries at 1150 °C [20]. Moreover, the strain rate played a significant role in the dynamic recrystallization process of GH690 alloy [23]. Furthermore, scholars have also devoted to improving the hot forming technique of superalloy [24–26]. With the neutron diffraction method, the residual stress in the Inconel 625 alloy tube was predicted [24]. By response surface methods to optimize the extrusion process for large-size thick-walled Inconel 625 alloy pipe, the best process parameter window was obtained [25]. The die surface was treated with shot peening to improve the die life [26]. Finally, studies have investigated the hot processing map of superalloys during hot deformation [27–30].

In this study, hot compression experiment of as-cast Inconel 625 alloy was implemented by the thermo-simulator system Gleeble-3500. The true stress–strain curves,

constitutive equation, the processing map and the effects of temperature and strain rate on the microstructural characteristic were established. The research results will provide a theoretical basis for the simulation optimization and numerical calculation of short processes and also lay the foundation for improving the current hot extrusion process or preparing a more excellent hot extrusion process.

2 Experimental

The material used in this experiment was Inconel 625 alloy provided by Jinchuan Nickel Alloy Co., Ltd., as shown in Fig. 2a, b. The chemical compositions of the Inconel 625 alloy are given in Table 1. The microstructure of the cross section of the alloy is observed by optical microscope (OM, XTZ-D), as illustrated in Fig. 2c, d.

The segregation phases of as-cast Inconel 625 alloy were investigated by differential scanning calorimeter (DSC, 404 F3 Pegasus[®]) and energy-dispersive spectrometer (EDS, SEM-6700F), as shown in Fig. 2e, f. There are some brittle Laves phases and carbides (MC) in the alloy by (Fig. 3b). The main elements of segregation phases are Nb, Cr, Mo, Al, Ti. The segregation coefficient (K) was calculated to represent the segregation degree of each element based on the result of EDS, as shown in Table 2. The segregation degree of elements can be sorted as $Nb > Mo > Ti > Al > Cr$.

In order to eliminate segregation and dendrite, the two-stage homogenization treatment of the as-cast Inconel 625 alloy was carried out. The scale of Laves phases simply decreased with increase in the homogenization treatment time, and the morphologies also changed, as shown in Fig. 3a–d. Laves phases are basically eliminated after 32-h homogenization treatment. The treatment process was at 1100 °C for 11 h and then heated to 1150 °C for 60 h. As shown in Fig. 3e, a mass of equiaxed crystal were

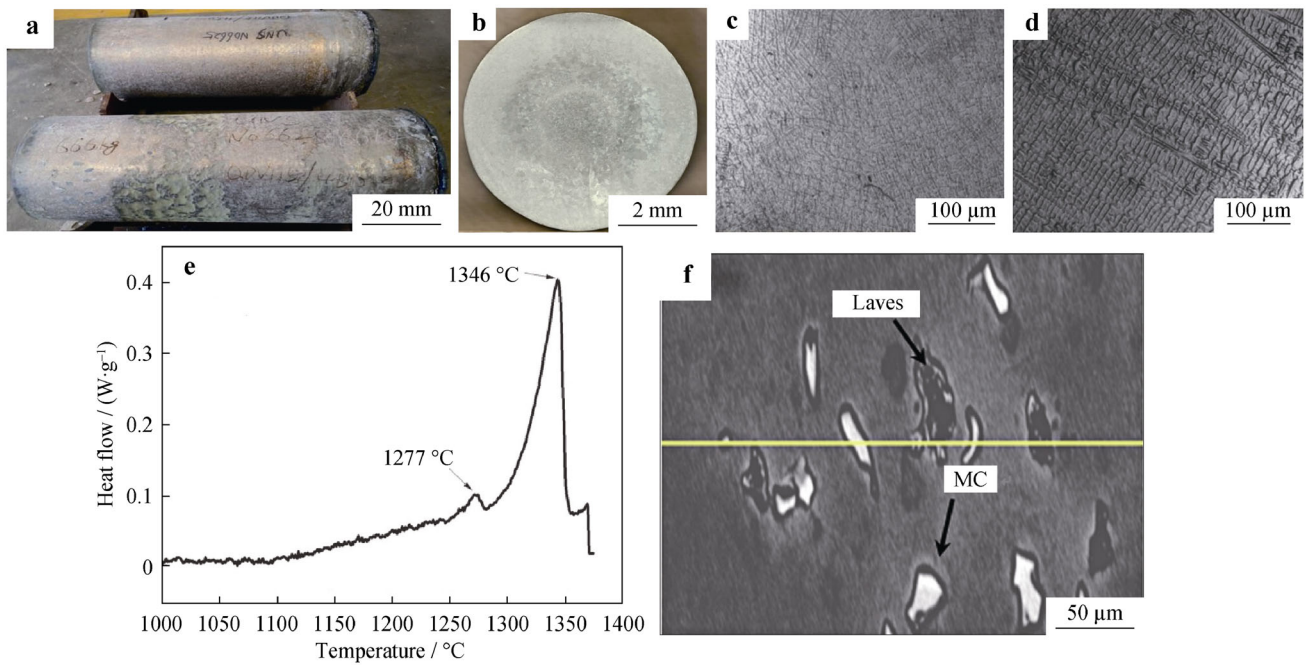


Fig. 2 Macroimages of **a** Inconel 625 alloy ingot and **b** its low-power macrostructure; as-cast OM images of Inconel 625: **c** intersecting surface and **d** longitudinal surface; segregation phases of as-cast Inconel 625 by **e** DSC and **f** EDS

Table 1 Major chemical compositions of Inconel 625 (wt%)

C	Cr	Ni	Co	Mo	Al	Fe	Ti	Nb	Si	Mn
0.042	21.77	60.63	0.19	8.79	0.21	3.68	0.40	3.75	0.12	0.20

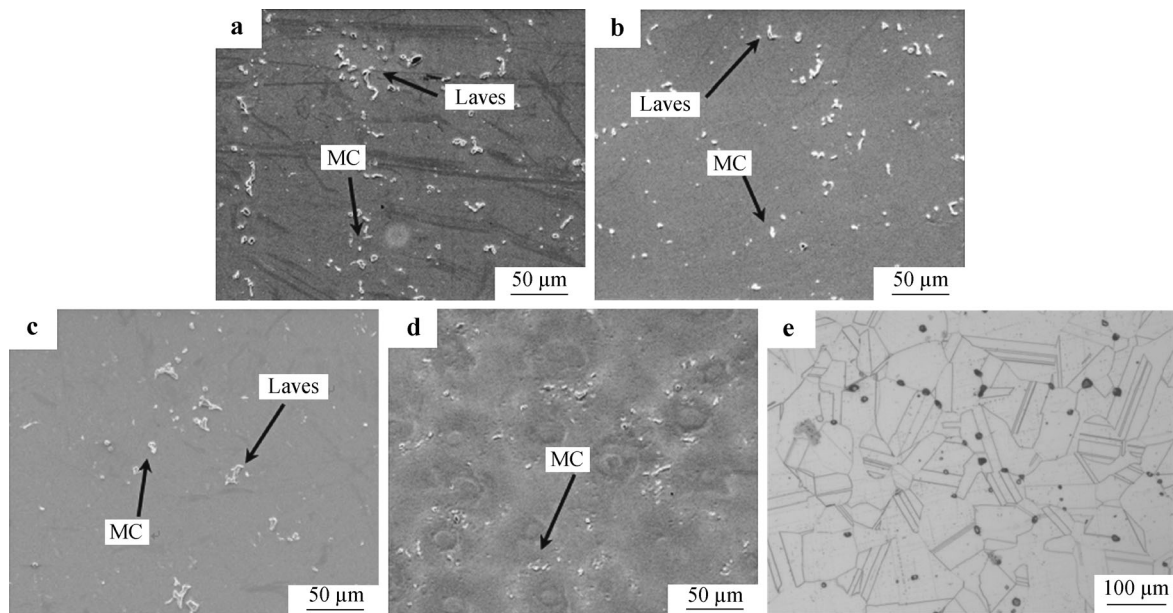


Fig. 3 Microstructure of as-cast Inconel 625 after homogenization treatment for different times: **a** 4 h, **b** 8 h, **c** 16 h and **d** 32 h; **e** OM image of Inconel 625 after homogenization treatment

Table 2 Main element content in dendrite and interdendrite (wt%)

Elements	Nb	Mo	Ti	Cr	Al
Dendrite	1.44	8.94	0.21	0.14	0.19
Interdendrite	4.54	16.24	0.33	17.68	0.27
K	3.15	1.81	1.57	0.73	1.42

observed, and some twins formed simultaneously during homogenization treatment.

The sample of alloy was cut into $\Phi 8 \text{ mm} \times 12 \text{ mm}$ and polished for one-way compression experiments on Gleeble-3500 hot simulation experimental machine. It was heated to the experimental temperature at a speed of $278 \text{ K} \cdot \text{s}^{-1}$, and the compression deformation was carried out at different strain rates after 3-min heat preservation. The deformation temperature of the hot simulation test was 900, 950, 1000, 1050, 1100, 1150 and $1200 \text{ }^\circ\text{C}$, respectively. The strain rate was 0.01, 0.10, 1.00 and 10.00 s^{-1} , and the maximum true strain was 0.7. After the hot compression, the samples were immediately water-cooled. Specially, to reduce the effect of friction on the stress state, graphite was applied at both ends of the specimen, and tantalum was added to the specimen. For convenience of electron backscatter distribution (EBSD, JSM-6700F) analysis, all specimens were ground to a thickness of 1–3 mm, and disks with 3 mm in diameter were punched out. Next, the samples were mechanically polished and then polished electrolytically with a solution of 20 ml $\text{H}_2\text{SO}_4 + 80 \text{ ml CH}_3\text{OH}$.

3 Results and discussion

3.1 True stress–strain curve

Figure 4 shows the true stress–true strain curve of the as-cast Inconel 625 alloy at different temperatures and strain rates. It can be found that the flow stress with deformation degree increases rapidly to a peak, then gradually decreases and finally tends to be stable, which accords with the rheological characteristic of low stacking fault energy (SFE) metals and also indicates the occurrence of dynamic recrystallization during hot deformation. At the same strain rate, the flow stress decreases with the increase in deformation temperature, and at the same temperature, the flow stress increases with the increase in strain rate.

When the strain rate of Inconel 625 is 0.01 and 1.00 s^{-1} , the stress–strain curves present serration after the rheological stress reaches the peak value. This is due to the interaction between the softening caused by dynamic recrystallization and the hardening caused by retransformation of the recrystallization grain. This phenomenon also indicates that dynamic recrystallization–deformation occurs repeatedly during the deformation process.

Obviously, the dynamic recovery and dynamic recrystallization appeared during hot compression deformation of the as-cast Inconel 625 alloy. In the initial stage, the dislocation density increases with the increase in strain, and the softening effect of Inconel 625 caused by dislocation cross-slip is not enough to compensate for the hardening effect caused by the increase in dislocation density, so that the flow stress increases quickly. Therefore, work hardening is dominant before reaching the peak stress. When the deformation is large enough to exceed a certain critical deformation amount, the dislocation density is also relatively high, the deformation storage energy will provide a driving force for recrystallization, and at this time, the softening effect caused by dynamic recrystallization gradually becomes dominant, but when the hardening caused by the retransformation of the grains and the softening caused by recrystallization reach a dynamic balance, the flow stress reaches a certain peak, and then, the curve enters a steady state.

3.2 Constitutive equations

The influence of the strain rate ($\dot{\epsilon}$) on the flow stress (σ) and temperature during hot compression of Inconel 625 can be represented by constitutive equations proposed [31]. Equation (1) is the general form of the constitutive relation of Arrhenius.

$$\dot{\epsilon} = A_1 [\sinh(\alpha\sigma)]^n \exp(-Q/RT) \quad (1)$$

Equation (1) can be expressed as different forms under different stress levels. The specific results are as follows:

$$\dot{\epsilon} = A_1 \sigma^{n_1} \exp(-Q/RT) \quad \text{when } \alpha\sigma \leq 0.8 \quad (2)$$

$$\dot{\epsilon} = A_2 \exp(\beta\sigma) \exp(-Q/RT) \quad \text{when } \alpha\sigma \geq 1.2 \quad (3)$$

$$\dot{\epsilon} = A [\sinh(\alpha\sigma)]^n \exp(-Q/RT) \quad \alpha\sigma \text{ is an arbitrary value} \quad (4)$$

Equation (2) is suitable for a low stress level, Eq. (3) is suitable for a high stress level, and Eq. (4) is suitable for all stress, where α , β and n_1 are the constants related to material, and $\alpha = \beta/n_1$; Q is the activation energy of deformation; R is the universal gas constant ($8.314 \text{ J} \cdot \text{mol}^{-1} \cdot \text{K}^{-1}$); T is the deformation temperature; A_1 , A_2 and A are the coefficients; and Q and A are independent of temperature. But such independence is not absolute and is restricted to the temperature range without phase transformation.

When the temperature is constant, Q , R , T and A are constants in Eqs. (2), (3). Equations (5), (6) are built by evaluating the natural logarithm of Eqs. (2), (3).

$$\ln \dot{\epsilon} = \ln A_1 + n_1 \ln \sigma - Q/RT \quad (5)$$

$$\ln \dot{\epsilon} = \ln A_2 + \beta\sigma - Q/RT \quad (6)$$

When T is certain, $\ln \dot{\epsilon}$ versus $\ln \sigma$ and $\ln \dot{\epsilon}$ versus σ are all linear relations on Eqs. (5) and (6). The peak stress of

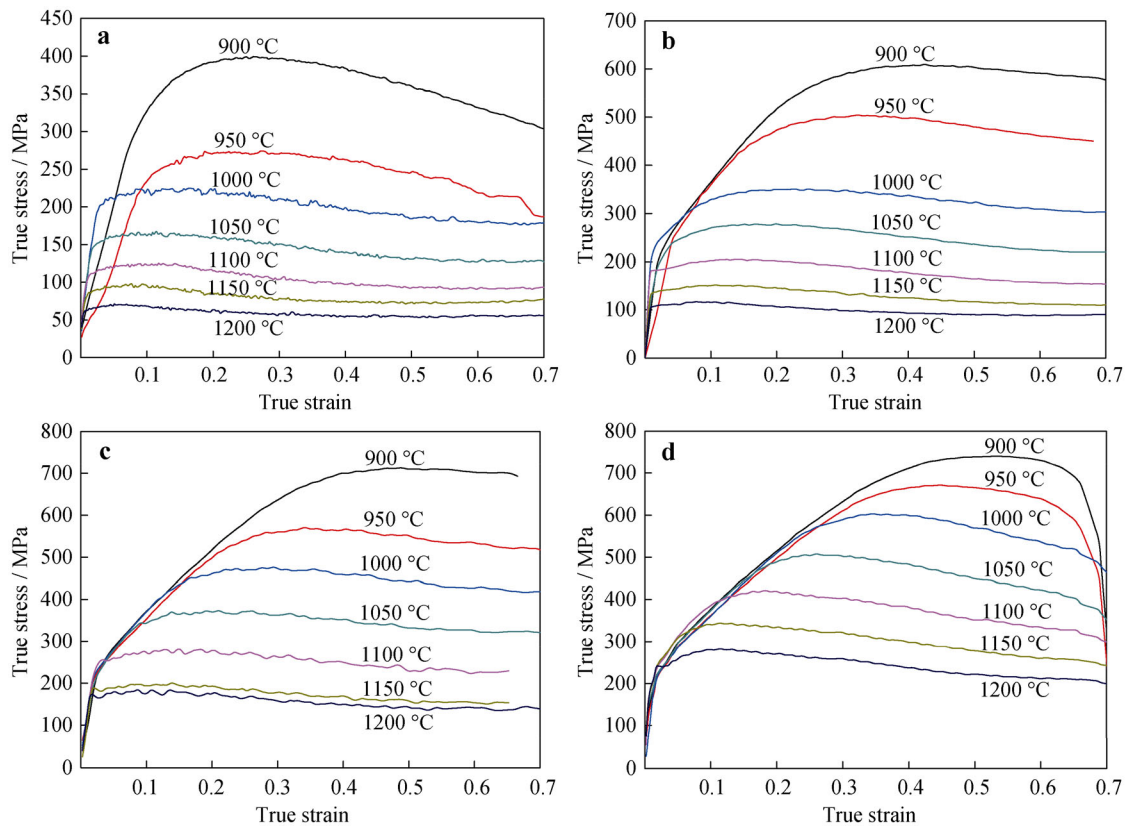


Fig. 4 True stress–strain curves of Inconel 625 at different strain rates and temperatures: **a** $\dot{\epsilon} = 0.01 \text{ s}^{-1}$, **b** $\dot{\epsilon} = 0.10 \text{ s}^{-1}$, **c** $\dot{\epsilon} = 1.00 \text{ s}^{-1}$, and **d** $\dot{\epsilon} = 10.00 \text{ s}^{-1}$

different deformation conditions is obtained, and the $\ln\sigma$ versus $\ln\dot{\epsilon}$ and σ versus $\ln\dot{\epsilon}$ linear relations are fitted, as shown in Fig. 5a, b. From Fig. 5a, n_1 is 7.01116. From Fig. 5b, β is 0.02343 MPa^{-1} . According to $\alpha = \beta/n_1$, α is 0.0033 MPa^{-1} . Evaluating the natural logarithm of Eq. (1) can obtain:

$$\ln \dot{\epsilon} = \ln A + n \ln \sinh(\alpha\sigma) - Q/RT \tag{7}$$

In a definite temperature, the calculation formula of Q is built by evaluating the partial differential equation of Eq. (7).

$$Q = R(\partial \ln \dot{\epsilon}) / (\partial \ln \sinh(\alpha\sigma))_T (\partial \ln \sinh(\alpha\sigma) / (\partial T^{-1}))_{\dot{\epsilon}} \tag{8}$$

The peak stress of different deformation conditions is taken to make $\ln \sinh(\alpha\sigma)$ versus $\ln \dot{\epsilon}$ and $\ln \sinh(\alpha\sigma)$ versus T^{-1} relation curves, as shown in Fig. 5c, d. The average of the slope of the two graphs is taken, and according to Eq. (8), the deformable activation energy (Q) of the as-cast Inconel 625 alloy is $473.713 \text{ kJ}\cdot\text{mol}^{-1}$. This value is nearly equal to that of forged Inconel 625 alloy ($Q = 420.85 \text{ kJ}\cdot\text{mol}^{-1}$ [1]). The value is higher compared with the reported values of other Ni-based superalloys such as Inconel 690, Inconel 718 and GH3535 [32].

Figure 5c, d shows the relationship between $\ln \sinh(\alpha\sigma)$, T and $\ln \dot{\epsilon}$. From Eq. (7), the relationship between $\ln \dot{\epsilon}$ and $\ln \sinh(\alpha\sigma)$ is linear. The average value of the slope of the straight line is n . The intercept of the straight line is $(Q/RT - \ln A)/n$. From Fig. 5a, b, n is 4.873, and A is 5.816×10^{17} . The constitutive equation of the as-cast Inconel 625 alloy is obtained as follows:

$$\dot{\epsilon} = 5.816 \times 10^{17} [\sinh(0.0033\sigma)]^{4.873} \times \exp(-473.713/RT) \tag{9}$$

To verify the accuracy of the constitutive equation, the peak stress at different temperatures and strain rates is calculated according to Eq. (9), and compared with the experimental results, as shown in Fig. 6. It can be seen from the graph that the maximum error is 17.4%, the minimum error is 0.168%, and the average error is 4.88%, so the predicted value is good agreement with the experimental value.

3.3 Processing map of as-cast Inconel 625

Processing maps are developed based on dynamic materials model (DMM) to represent the material response in terms of specific microstructural processes. In the process

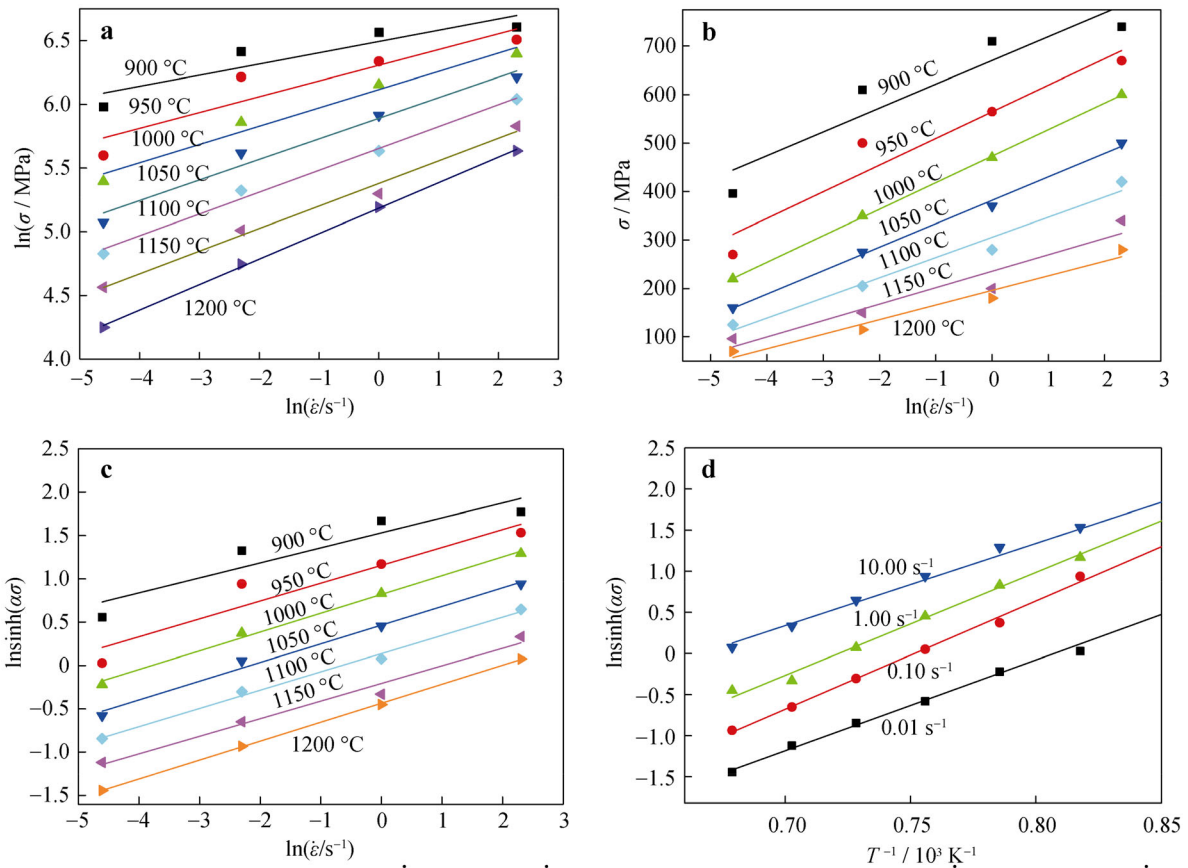


Fig. 5 Relationship between peak stress and strain rate: **a** $\ln\sigma$ – $\ln\dot{\epsilon}$ and **b** σ versus $\ln\dot{\epsilon}$; relationship between $\ln\sinh(\alpha\sigma)$, T and $\ln\dot{\epsilon}$: **c** $\ln\sinh(\alpha\sigma)$ versus $\ln\dot{\epsilon}$ and **d** $\ln\sinh(\alpha\sigma)$ versus T^{-1}

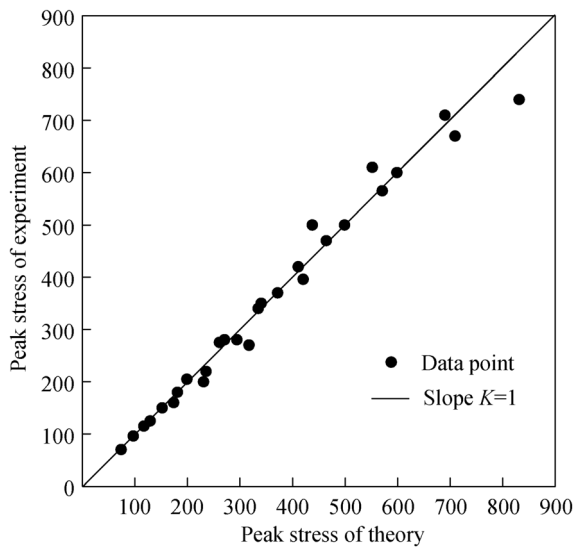


Fig. 6 Comparison of predicted peak stress and experimental stress

of hot deformation, when the deformation temperature and the strain rate are certain, the constitutive relation of the material can be expressed as:

$$\sigma = K\dot{\epsilon}^m \tag{10}$$

where m is the strain rate sensitive factor; J is the consumption energy by the microstructure evolution of a material during plastic deformation; and G is the Gibbs free energy. m is defined as:

$$m = dJ/dG = (\dot{\epsilon}d\sigma)/(\sigma d\dot{\epsilon}) = (d \ln \sigma)/(d \ln \dot{\epsilon}) \tag{11}$$

where J_{\max} is the linear energy by the microstructure evolution of a material during plastic deformation. A set of cubic splines at different strains (0.1, 0.3, 0.5) can be obtained by interpolating all the flow stress–strain curves. Then, the derivative of the spline fit calculates the strain rate sensitivity factor m . The power dissipation coefficient (η) is given as

$$\eta = J/J_{\max} = (m\sigma\dot{\epsilon}/(m + 1))/(\sigma\dot{\epsilon}/2) = 2m/(m + 1) \tag{12}$$

Based on the principle of maximum entropy production, Zeigler puts forward the criterion of rheological instability (ζ) of materials at high temperature, which is expressed as:

$$\zeta(\dot{\varepsilon}) = (\partial \ln[m/(m+1)]) / (\partial \ln \dot{\varepsilon}) + m \quad (13)$$

The processing map of the different strains (0.1, 0.3, 0.5) constructed by overlaying the instability map onto the power dissipation maps is shown in Fig. 7. The dissipation factor increases exponentially with the increase in the temperature; however, it was little changed with the strain increasing. When the strain is small, the instability zone covers a lot of domains of processing map. With the strain increasing, the instability zone gradually transits to low-temperature and low strain rate region. The peak efficiency of 0.49 occurs at the temperature of 1423 K and strain rate of 10.00 s^{-1} . The effect of strain rate on dissipation factor for as-cast Inconel 625 alloy is much greater than that of temperature.

As shown in Fig. 7c, the as-cast Inconel 625 alloy has two main instability zones at the strain of 0.5. The first zone is located in the strain rate range of $0.022\text{--}1.580 \text{ s}^{-1}$ and the temperature range of $900\text{--}1020 \text{ }^\circ\text{C}$. This is because recrystallization is a hot activation process. When the temperature is low, the storage energy inside the crystal is low, which is not enough to cause complete recrystallization. Therefore, the inhomogeneous deformation is serious, resulting in rheological instability. The second zone is located in the strain rate range of $0.01\text{--}0.10 \text{ s}^{-1}$ and the temperature range of $1125\text{--}1175 \text{ }^\circ\text{C}$. On the one hand, due to the higher temperature and activation energy, grain boundaries and phase boundaries are easy to slide. Many dislocations result in stress concentration in the grain and phase boundaries, leading to occurrence of discontinuous dynamic recrystallization. On the other hand, due to the longer deformation time at the lower strain rate, grains tend to be nonuniform, which results in rheological instability.

There are two main stable zones in the processing map of the as-cast Inconel 625 alloy at different strains (0.1, 0.3, 0.5). The first stable zone with the dissipation efficiency of $0.07\text{--}0.28$ is located in the strain rate range of $1.58\text{--}10.00 \text{ s}^{-1}$ and the temperature range of $900\text{--}1025 \text{ }^\circ\text{C}$. The microstructural evolution of alloy in this zone is

dominated by dynamic recovery, because of in this zone without enough time recrystallization or only a small amount of recrystallization nucleation. The second stable zone with the dissipation efficiency of greater than 0.3 is located in the strain rate range of $1.00\text{--}10.00 \text{ s}^{-1}$ and the temperature range of $1050\text{--}1200 \text{ }^\circ\text{C}$. The peak efficiency is 0.49 at the temperature of $1150 \text{ }^\circ\text{C}$ and the strain rate of 10.00 s^{-1} . The grain boundary migration ability is improved because the atomic diffusion rate is accelerated. Meanwhile, the high strain rate makes the grains hard to grow and can get fine and uniform recrystallized grains.

The evolution of microstructure of the as-cast Inconel 625 alloy was analyzed to verify the accuracy of the processing map. The typical microstructures under different temperatures and strain rate of 1.00 s^{-1} were obtained by EBSD analysis, as shown in Fig. 8a–g. Figure 8 a–d, f, g marks the grains with diameter between 0 and $10 \text{ }\mu\text{m}$ by different colors at different temperatures; Fig. 8e shows the grains with diameter between 0 and $5 \text{ }\mu\text{m}$. The microstructural evolution of instability zones is the dissipation efficiency of below 0.21, as shown in Fig. 8a–d. The dynamic recrystallization is incomplete, and the residual initial grains elongate against to the compress direction. The original grains are compressed into ribbons that are decorated with chains of ultrafine grains. The formation of new grains takes place along the bulging grain boundaries. The phenomenon can be attributed to no enough energy to grow up at the lower temperature, resulting in the restriction of the initial grain boundary migration. As shown in Fig. 8a–g, it is founded that the content of fine DRX grains increases gradually, and the average grain size decreases first and then increases. One is that the imbalance between the newly formed non-distorted DRX grain and the original grain of the high dislocation density will lead to the growth of grain. Second, the high temperature and deformation rate will lead to faster grain boundary migration, thus promoting grain growth. The perfect dynamic recrystallization occurs at $1100 \text{ }^\circ\text{C}$ with the dissipation efficiency of 0.28, as illustrated in Fig. 8e. These microstructure in the

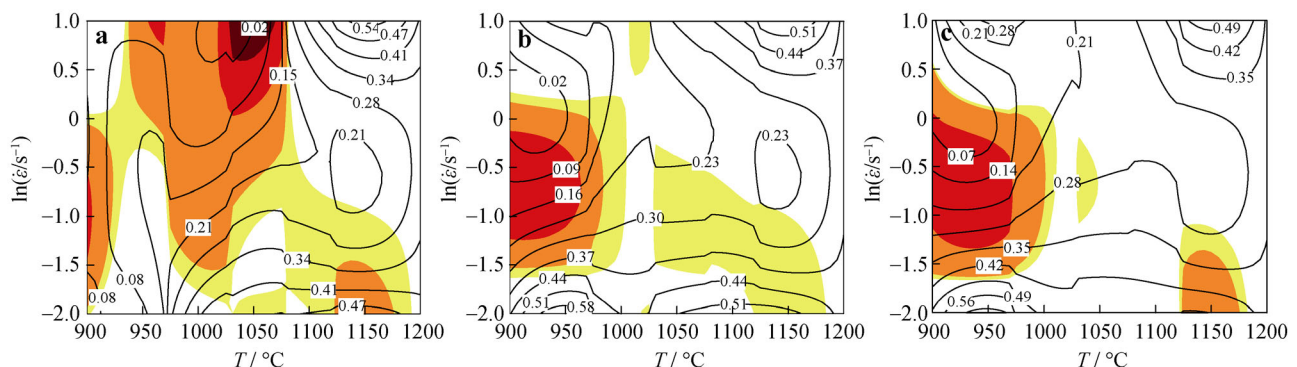


Fig. 7 Processing map of the as-cast Inconel 625 alloy at different strains: **a** $\varepsilon = 0.1$, **b** $\varepsilon = 0.3$, and **c** $\varepsilon = 0.5$

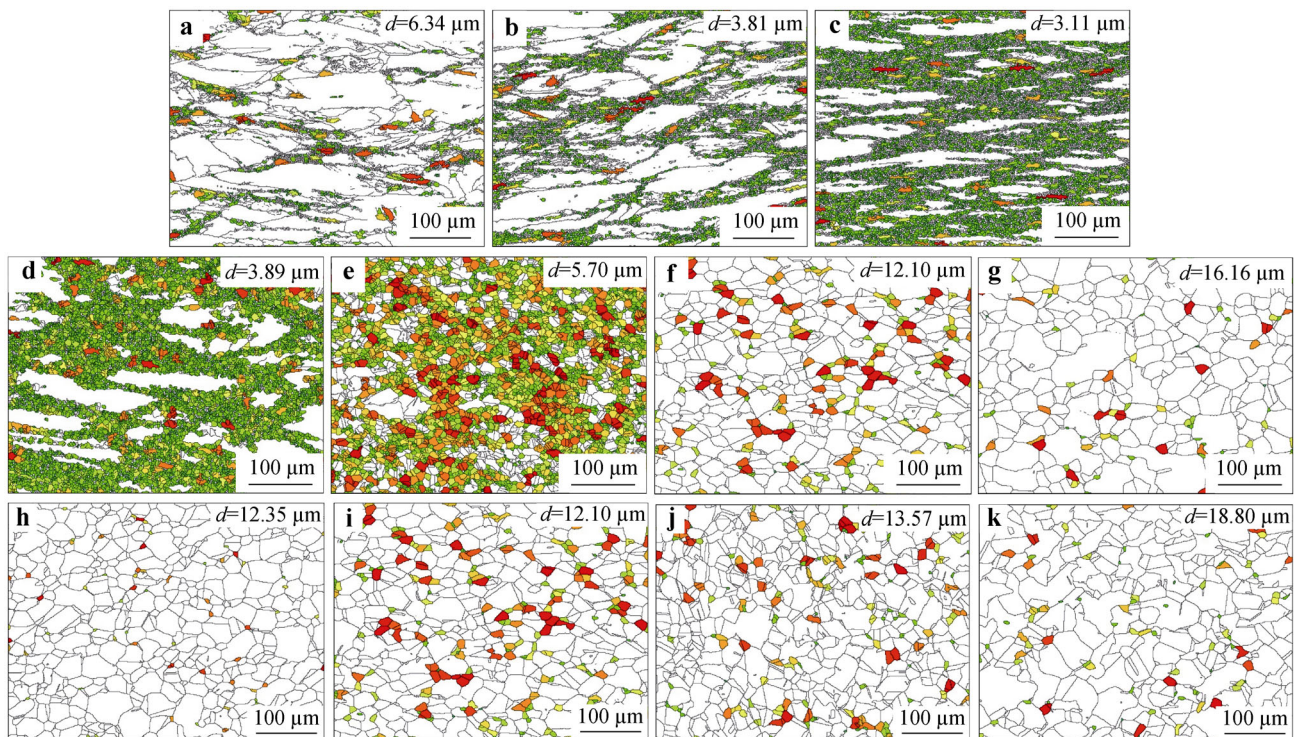


Fig. 8 EBSD images of Inconel 625 at different temperatures and 1.00 s^{-1} : **a** 900 °C, **b** 950 °C, **c** 1000 °C, **d** 1050 °C, **e** 1100 °C, **f** 1150 °C and **g** 1200 °C; EBSD images of Inconel 625 at different strain rates and 1150 °C: **h** 10.00 s^{-1} , **i** 1.00 s^{-1} , **j** 0.10 s^{-1} and **k** 0.01 s^{-1}

dissipation efficiency of below 0.28 shows that the deformation mechanism of the as-cast Inconel 625 alloy is dynamic recovery and partial recrystallization, which means that the soften effect is much weaker than work-hardening effect.

The typical microstructures under different strain rates are obtained by EBSD analysis at 1150 °C, and the grains with diameter between 0 and 10 μm are marked with different colors, as shown in Fig. 8h–k. These microstructure shows that the perfect dynamic recrystallization occurs in all specimens. Compared with Fig. 8k (the dissipation efficiency of 0.28), the recrystallization zone and the new grain sizes shown in Fig. 8h are obviously smaller. This is ascribed to no enough time to grow up at the higher strain rate. As the strain rate increases, the microstructure is more uniform and the local grain growth is suppressed. It is found that the uniform equiaxed grains are formed through dynamic recrystallization in the peak dissipation efficiency of 0.49, as shown in Fig. 8h. From Fig. 8, the grain sizes and the volume fraction of dynamic recrystallization are decided by the temperature rather than the strain rate, and the grain sizes of specimens increase with temperature increasing and strain rate decreasing. The deformation mechanism of the as-cast Inconel 625 alloy is dynamic recrystallization with the dissipation efficiency of above 0.28, and the soften effect is much greater than work-

hardening effect. The trend is consistent with the conclusion from Fig. 3a–d.

Through analyzing the segregation phase of as-cast Inconel 625 by DSC and EDS, the Laves phases were found. In order to eliminate segregation and dendrite, Laves phases are basically eliminated after 32-h homogenization treatment. It can be found that the flow stress with deformation degree increases rapidly to a peak, then gradually decreases and finally tends to be stable. Furthermore, the hot deformation behavior is described by constitutive equation. The optimal hot processing interval is obtained by processing map and verified by the microstructure evolution. According to the microstructure figure obtained by EBSD, the grain size was uniform and the structure was stable in the optimal processing interval.

4 Conclusion

In this study, high-temperature deformation behavior and processing map of the as-cast Inconel 625 alloy were studied in the temperature range of 900–1200 °C and strain rate range of 0.01 – 10.00 s^{-1} through hot compression tests on a thermo-mechanical simulator. The flow stress of cast Inconel 625 alloy with deformation degree increases rapidly to a peak, then gradually decreases and finally tends

to be stable, conforming to the rheological characteristic of low stacking fault energy metal. The deformable activation energy of the as-cast Inconel 625 alloy is $473.713 \text{ kJ}\cdot\text{mol}^{-1}$. The constitutive equation of the alloy is as $\dot{\epsilon} = 5.816 \times 10^{17} [\sinh(0.0033\sigma)]^{4.873} \times \exp(-473.713/RT)$. The processing map of the as-cast Inconel 625 alloy has two main instability zones, which are low-temperature region (strain rate of $0.022\text{--}1.580 \text{ s}^{-1}$, temperature range of $900\text{--}1020 \text{ }^\circ\text{C}$) and high-temperature region (strain rate of $0.01\text{--}0.10 \text{ s}^{-1}$, temperature range of $1125\text{--}1175 \text{ }^\circ\text{C}$). The optimum process parameters of the as-cast Inconel 625 alloy are high strain rate region (temperature of $1100\text{--}1200 \text{ }^\circ\text{C}$, strain rate of $1.00\text{--}10.00 \text{ s}^{-1}$) with the dissipation efficiency of above 0.28, where the perfect dynamic recrystallization occurs and fine grain structure is obtained.

Acknowledgements This study was financially supported by the National Natural Science Foundation of China (Nos. 51665032 and 51664041), the Science Foundation for Distinguished Young Scholars of Gansu Province (No. 18JR3RA134).

References

- Zhou HT, Liu RR, Liu ZC, Zhou X, Peng QZ, Zhong FH, Peng Y. Hot deformation characteristics of GH3625 and development of a processing map. *J Mater Eng Perform*. 2013;22(9):2515.
- Rodriguez D, Merwin A, Karmiol Z, Chidambaram D. Surface chemistry and corrosion behavior of Inconel 625 and 718 in subcritical, supercritical, and ultrasupercritical water. *Appl Surf Sci*. 2017;404(15):443.
- Zuo Q, Liu F, Wang L, Chen CF, Zhang ZH. Prediction of hot deformation behavior in Ni-based alloy considering the effect of initial microstructure. *Prog Nat Sci Mater Int*. 2015;25(1):66.
- He J, Sandström R, Notargiacomo S. Low-cycle fatigue properties of a nickel-based superalloy Haynes 282 for heavy components. *J Mater Eng Perform*. 2017;26(5):2257.
- Wang J, Dong J, Zhang M, Xie X. Hot working characteristics of nickel-base superalloy 740H during compression. *Mater Sci Eng A*. 2013;566(2):61.
- Pan Y, Guan WM. Probing the balance between ductility and strength: transition metal silicides. *Phys Chem Chem Phys*. 2017;19:19427.
- Shi ZX, Yan XF, Duan CH, Zhao MH. Effect of strain rate on hot deformation characteristics of GH690 superalloy. *Trans Nonferr Met Soc China*. 2017;27(3):538.
- Chaudhuri A, Raghupathy Y, Srinivasan D, Suwas S, Srivastava C. Microstructural evolution of cold-sprayed Inconel 625 superalloy coatings on low alloy steel substrate. *Acta Mater*. 2017;129:11.
- Chen X, Qi YG, Shi XN, Xie BC, Ning YQ. Behaviors and model of dynamic recrystallization of nickel-based superalloy IN718Plus. *Chin J Rare Met*. 2019;43(12):1260.
- Gao B, Wang L, Liang T, Liu Y, Song X, Qu J. Plastic deformation behavior of directionally solidified U720Li alloy at elevated temperature. *Acta Metall Sin*. 2016;52(4):437.
- Liu DX, Cheng XW, Zhang X, Ding YT. Effects of heating and hot extrusion process on microstructure and properties of Inconel 625 alloy. *J Wuhan Univ Technol*. 2016;31(6):1368.
- Liang XH, Zhou KS, Liu M, Deng CG. Recrystallization on interface between NiCoCrAlYTa coating and nickel-based super-alloy. *Rare Met Mater Eng*. 2009;38(3):545.
- Liu M, Zheng WJ, Xing JZ, Song ZG, Pu EX, Feng H. Grain growth behavior of Inconel 625 superalloy. *J Iron Steel Res Int*. 2016;23(10):1111.
- Gong ZH, Yang G, Ma LT, Wang L. Precipitation phases and mechanical properties of GY200 Ni-based alloy for blade with W and Mo addition. *Chin J Rare Met*. 2017;38(9):83.
- Dang L, Yang H, Guo LG, Shi L, Zheng WD, Zhang J. Extrusion limit map of large-scale thick-walled Inconel 625 alloy pipe using FE method. *Rare Met Mater Eng*. 2014;43(9):2130.
- Jiang P, Yuan YX, Xiao SJ, Wu WP, Wang ZZ, Ding JH, Jiang JJ. Microstructure and mechanical properties of multiphase V-Ti-Ni hydrogen separation alloys. *Rare Met Mater Eng*. 2018;47(8):2537.
- Qiu X, Yang Q, Guan K, Bu F, Cao ZY, Liu YB, Meng J. Microstructures and tensile properties of Mg-Zn-(Gd)-Zr alloys extruded at various temperatures. *Rare Met*. 2017;36(12):962.
- Wang RD, Hu Q, Zhang SM, Zhang FW, Lu CT, Wang ZG. Properties of (Fe-B)-doped Sn-1.0Ag-0.5Cu solders prepared by mechanical alloying. *Rare Met*. 2019;38(7):665.
- Yue X, Li J, Wang X. The microstructure of a single crystal superalloy after different aging heat treatments. *Rare Met*. 2018; 37(1):210-6.
- Gao Z, Jia Z, Ji J, Liu D, Guo T, Ding Y. Texture evolution and dislocation behavior in a nickel-based superalloy during hot compression. *Adv Eng Mater*. 2020;22(3):1438.
- Zhang W, Liu L. Solidification microstructure of directionally solidified superalloy under high temperature gradient. *Rare Met*. 2012;31(6):541.
- Jia Z, Gao Z, Ji J, Liu D, Guo T, Ding Y. Evolution of twin boundaries and contribution to dynamic recrystallization and grain growth of Inconel 625. *Adv Eng Mater*. 2019;21(9):1438.
- Shi ZX, Yan XF, Duan CH, Zhao MH. Effect of strain rate on hot deformation characteristics of GH690 superalloy. *Trans Nonferr Met Soc*. 2017;27(3):538.
- Jia Z, Gao Z, Ji J, Liu D, Guo T, Ding Y. Study of the dynamic recrystallization process of the Inconel 625 alloy at a high strain rate. *Materials*. 2019;12(3):510.
- Guo LG, Dang L, Yang H, Zhang J, Zheng WD. Identification of processing window for extrusion of large thick-walled Inconel 625 alloy pipes using response surface methodology. *Trans Nonferr Met Soc*. 2016;26(7):1902.
- Jia Z, Ji JJ. Influence analysis of shot peening on hot forging die. *Int J Adv Manuf Technol*. 2017;90(5-8):1779.
- Hu XA, Yang XG, Shi DQ, Yu HC, Ren TT. Constitutive modeling of a directionally solidified nickel-based superalloy DZ125 subjected to thermal mechanical creep fatigue loadings. *Rare Met*. 2019;38:922.
- Wang RN, Xu QY, Liu BC. A model for simulation of recrystallization microstructure in single-crystal superalloy. *Rare Met*. 2018;37(12):1027.
- Li FL, Fu R, Feng D, Tian ZL. Hot workability characteristics of Rene88DT superalloy with directionally solidified microstructure. *Rare Met*. 2015;34(1):1.
- Chen JY, Cao LM, Xue M, Liu LJ. Microstructure and stress-rupture property of an experimental single crystal Ni-base superalloy with different heat treatments. *Rare Met*. 2014;33(2): 144.
- Sellars CM, McEgart WJ. On the mechanism of hot deformation. *Acta Metall*. 1966;14(9):1136.
- Ji Y, Qu S, Han W. Hot deformation and processing map of GH3535 superalloy. *Trans Nonferr Met Soc*. 2015;25(1):88.